Effect of the Spherical Indenter Tip Assumption on the Initial Plastic Yield Stress

Li Ma, Lyle Levine, Ron Dixson, Douglas Smith and David Bahr

Additional information is available at the end of the chapter

http://dx.doi.org/10.5772/48106

1. Introduction

Nanoindentation is widely used to explore the mechanical properties of small volumes of materials. For crystalline materials, there is a growing experimental and theoretical interest in pop-in events, which are sudden displacement-burst excursions during load-controlled nanoindentation of relatively dislocation-free metals. The first pop-in event is often identified as the initiation of dislocation nucleation, and thus the transition from purely elastic to elastic/plastic deformation. The maximum shear stress at this first pop-in event, or the onset of plastic yielding, is generally found to be close to the theoretical strength of the material and is frequently estimated from Hertzian elastic contact theory. However, an irregular indenter tip shape will significantly change the stress distribution in magnitude and location, and therefore the maximum shear stress, from a Hertzian estimation. The aim of this chapter is to state the challenges and limitations for extracting the initial plastic yield stress from nanoindentation with the spherical indenter tip assumption. We assess possible errors and pitfalls of the Hertzian estimation of initial plastic yield at the nanoscale.

2. Background

Instrumented nanoindentation has been widely used to probe small scale mechanical properties such as elastic modulus and hardness over a wide range of materials and applications (Doerner & Nix, 1986; Fisher-Cripps, 2002; Oliver & Pharr, 1992, 2004). The response of a material to nanoindentation is usually shown by plotting the indentation load, P, as a function of the indenter penetration depth, h.

2.1. Nanoindentation of crystalline materials

For crystalline materials, nanoindentation can be used to study defect nucleation and propagation events, which are detected by discontinuities in the load-depth relationship.

INTECH
open science | open minds

Generally, there are three types of discontinuities as illustrated in Fig.1. First are "pop-in" events (as shown in Fig. 1a), which are sudden displacement excursions into the target materials during load-controlled nanoindentation of relatively dislocation-free metals. Pop-ins were first observed and associated with dislocation nucleation, or the sudden onset of plasticity, by Gane and Bowde in 1968 (Gane & Bowden, 1968) using fine stylus indentation of metal crystals. Pop-ins may also be associated with crack nucleation and propagation (Morris et al., 2004; Jungk et al., 2006), phase transformations (Page et al., 1992), and mechanically induced twinning (Bradby et al., 2002; Misra et al., 2010).

The second type of discontinuity is a "pop-out" event (as shown in Fig. 1b), which is a discontinuous decrease in the indentation displacement, usually during unloading. Pop-outs may also be ascribed to dislocation motion (Cross et al., 2006) and phase transformations (Juliano et al., 2004; Ruffell et al., 2007; Haq et al., 2007; Lee & Fong, 2008). A lower unloading rate or a higher maximum indentation load promotes the occurrence of a pop-out (Chang & Zhang, 2009).

The third type of load-depth discontinuity is the "load drop" found during a displacement-controlled experiment (Kiely & Houston, 1998; Warren et al., 2004), as shown in Fig. 1c. A molecular dynamics study showed that load drops are associated with local rearrangements of atoms (Szlufarska et al., 2007).
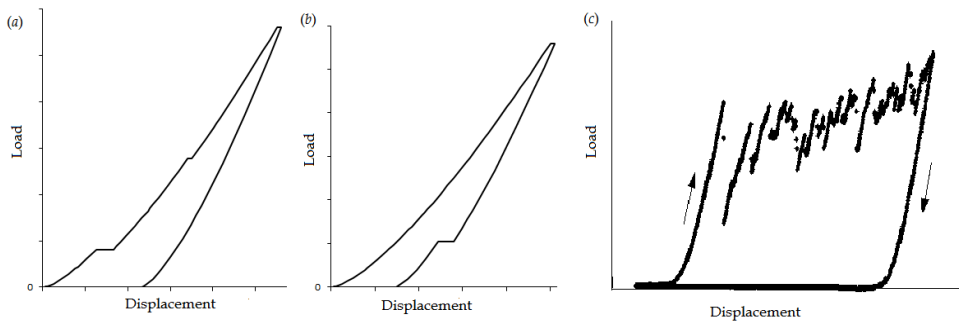

Figure 1. Schematic diagram of nanoindentation load displacement curve illustrating the (a) pop-in, (b) pop-out, and (c) load-drop behaviors.

2.2. Dislocation nucleation stress

Quantitative study of these nanoindentation phenomena requires reasonable estimates of the stresses that drove the particular event. Here, attention is focused on yield in metallic crystals. It is believed that the first pop-in event is most frequently the result of the initiation of dislocation nucleation, and thus the transition from purely elastic to elastic/plastic deformation (Gouldstone et al., 2000; Kelchner et al., 1998, 2009; Suresh et al., 1999; Li et al., 2002; Lorenz et al., 2003; Minor et al., 2004; Manson et al., 2006; Nix et al., 2007). The load-displacement curve before the pop-in occurs is often fully reversible, and is usually interpreted using the Hertzian contact theory (Johnson, 1999),

$$P = \frac{4}{3}\bar{E}_{R}R^{1/2}h^{3/2} \; , \tag{1}$$

where R is the indenter tip radius and

$$\bar{E}_{R} = \left[\left(1-v_{I}^{2}\right)\big/E_{I} + \left(1-v_{S}^{2}\right)\big/E_{S}\right]^{-1}$$

is the contact elastic modulus between the indenter (I) and specimen (S). In this case, the deformation is purely elastic prior to the first pop-in; if the indenter tip is unloaded before the first pop-in, atomic force microscopy (AFM) images show no indent on the specimen surface, whereas, if unloading occurs after the pop-in, a residual indent is observed (Chiu & Ngan, 2002; Schuh & Lund, 2004).

Nanoindentation pop-in tests can be a powerful tool for studying homogeneous and heterogeneous dislocation nucleation. When a pop-in event is caused by the sudden onset of crystal plasticity, whether through dislocation source activation (Bradby & Williams, 2004; Schuh et al., 2005) or homogeneous dislocation nucleation (Bahr et al., 1998; Chiu & Ngan, 2002), the maximum stress at the yield event is generally interpreted as the maximum shear stress in the body (Minor et al., 2006). This maximum shear stress, τ_{MAX}, at the first pop-in load, P_{CRIT}, is generally estimated from elastic contact theory (Johnson, 1999) as

$$\tau_{MAX} = 0.31\left[\frac{6\bar{E}_{R}^{2}}{\pi^{3}R^{2}}\right]^{\frac{1}{3}}P_{CRIT}^{\frac{1}{3}} \tag{2}$$

For a variety of materials, when the first pop-in occurs, the maximum shear stress in the specimen is in the range of G/30 to G/5, where G is the shear modulus; this stress is very close to the theoretical strength calculated by the *ab initio* method (Van Vliet et al., 2003; Ogata et al., 2004).

A recent study using molecular dynamics simulations found that the stress components other than the resolved shear stress also affect the dislocation nucleation process (Tschopp & McDowell, 2005; Tschopp et al., 2007). Based on an anisotropic elasticity analysis, Li et al. (2011) derived in closed form the stress fields under Hertzian contact theory and computed the indentation Schmid factor as a ratio of the maximum resolved shear stress to the maximum contact pressure.

2.3. Indenter tip shape

It must be emphasized that equations (1) and (2) are restricted to spherical indentation and cannot be applied to arbitrary geometries. Thus, the radius of the indenter probe is an essential component for estimating dislocation nucleation shear stress inferred from spherical indentation responses. Also, access to the nanometer length scales needed to find a dislocation-free region in a metallic crystal may require very small radii. Here, experimentalists can take advantage of the imperfect manufacture of nominally sharp geometries, such as the three-sided pyramidal Berkovich indenter. The most common view

is that the manufacturing process produces an approximately spherical cap on the apex of the indenter tip. The radius of the assumed spherical tip is generally obtained from the tip manufacturer, AFM, scanning electron microscopy (SEM), or by a Hertzian fit to the elastic load-displacement data (Chiu & Ngan, 2002; Constantinides et al., 2007; Gerberich et al., 1996; Gouldstone et al., 2000).

2.4. Challenge of extracting dislocation nucleation stress from nanoindentation

It is known that real pyramid indenter tips may have irregular shapes, especially at the nanometer-scale where the first pop-in event occurs. Previous finite element analysis (FEA) simulations and combined experimental and FEA studies have shown that even a highly irregular probe (which cannot simply be decomposed into "sphere" and "cone") will produce an elastic load-displacement relationship that could be perceived as having been from a spherical contact (Ma & Levine, 2007; Ma et al., 2009, 2012). Unsurprisingly, the simulations showed that the irregular shape generated shear stresses in the body that were significantly different, both in magnitude and location, from those produced by a true spherical probe. Using the common Hertzian spherical approximation to interpret experimental data can lead to a substantial underestimation of the maximum shear stress in the body at the initiation of plasticity. An assessment of the potential errors in experimental estimates of nucleation stresses is critical, especially in materials that exhibit the elastic-plastic transition at small indentation depth. We need to accurately measure the three dimensional shape of the true indenter, prepare a sample that has both low dislocation density and a smooth surface, and conduct nanoindentation experiments with accurate load and displacement measurements. In addition, several groups have reported that the rate at which the indenter tip penetrates the specimen can have a significant effect on the plastic deformation mechanisms in materials as diverse as Si (Jang et al., 2005), single-crystal Ni_3Al (Wang et al., 2003) and single-crystal Al_2O_3 (Mao et al., 2011). In the rest of this section, we will describe some of the difficulties involved in these measurements and some of the directions we, and others, are pursuing to overcome them.

2.4.1. Direct measurement of three dimensional shape of true indenter

There has been interest in direct measurement of the indenter geometry for at least two decades. At the larger micrometer to millimeter scale of Rockwell hardness indenters, for example, NIST has played a leading role in the drive toward indenter standardization (Song et al., 1997). Direct metrology of indenter geometry, using well-calibrated stylus profilers, is the most effective method at these size scales, and it is able to provide uncertainties low enough to support the uncertainty goals in Rockwell hardness measurements themselves.

For instrumented nanoindentation, however, the smaller sizes greatly increase the challenges to direct metrology of the indenter geometry. In the 1980s, Doerner and Nix (Doerner & Nix, 1986) measured the geometry of a Vickers indenter with transmission electron microscopy (TEM) by using a process for making carbon replicas of indents on soft surfaces.

In the early 90s, the work of Oliver and Pharr (Oliver & Pharr, 1992) led to the now prevalent method of inferring tip area from indentations on a sample of known modulus (McElhaney et al., 1998). By the late 90s, interest in the direct metrology of indenters using scanned probe microscopes was growing.

In 1998, researchers at PTB (Hasche et al., 1998) used scanned probe microscopy to characterize the geometry of Vickers microhardness indenters. Subsequently, they expanded their efforts to include Berkovich indenters (Herrmann et al., 2001).

During the following decade, work in this area significantly increased. Aldrich-Smith and coworkers (Aldrich-Smith et al., 2005) at the National Physical Laboratory (NPL) of the UK used a traceably-calibrated AFM to measure the tip area function of indenters, and compared these with the area function derived from indentation.

VanLandingham and coworkers (VanLandingham et al., 2005) undertook a detailed investigation of indenter tip shape as measured by AFM compared with that inferred by indentation on fused silica. They also developed a heuristic model of the indenter geometry as a spherical cap in place of an ideal apex on the Berkovich pyramid. For a vertical calibration range of less than 1 μm, they concluded that measurement of tip area by AFM typically performed better than the indentation method.

In 2007, McMinis and coworkers (McMinis et al., 2007) used the heuristic two-term polynomial model to fit the tip area function measured by AFM. The motivation for their model also was the assumption of an approximately spherical cap. However, in contrast with VanLandingham and coworkers, McMinis, et al. (2007) focussed on much smaller indentation depths – and found excellent performance of their approach relative to indentation on fused silica – particularly for depths less than 7 nm.

More recently, Munoz-Paniagua and coworkers (Munoz-Paniagua et al., 2010) effectively used a hyperbolic model to fit the geometry of worn Berkovich indenters measured by AFM. One of their illuminating observations was that the use of the indentation-derived shape area function could result in errors of the same scale as the assumption of an ideal Berkovich geometry.

Measurement of nanoindenter tip geometry by AFM remains an area of active investigation, and the next decade may well be more prolific than the last in terms of new insights and refinement of methods.

2.4.2. Sample preparation

It has been clearly demonstrated that irregularities in the tip shape can produce substantial changes in the perceived internal shear stresses. It is likely that irregularities in the sample topography can produce similar problems, and quantitative assessments of this affect are planned. In the meantime, it is important to minimize these problems by using samples that are as flat as possible. Unfortunately, mechanical polishing (even using colloidal silica) of face-centered cubic (FCC) metals can introduce substantial numbers of dislocations into the near-surface region of the sample which can adversely affect the measurement. The following

procedure has been effective at largely eliminating these problems for Ni specimens, but quantitative assessments still need to be done. The measurements described in the next section used tungsten specimens, which are less prone to damage during polishing.

We start with a {111}-oriented, chemi-mechanically polished, metal single crystal that is acquired from a commercial vendor. Optical microscopy generally shows no scratches and an apparently perfect mirror finish. Further characterization using optical interferometry and AFM have demonstrated that these samples have a surface roughness, R_q, of about 2.5 nm and exhibit numerous small scratches that are about 20 nm deep. To relieve any residual stresses and decrease the dislocation density of the sample, the Ni single crystal is slowly heated to 850 °C in ultra-high-vacuum and annealed at this temperature for about 140 h before slow cooling back to room temperature.

Remarkably, optical microscopy of the annealed sample shows numerous long, straight ridges that resemble reversed polishing scratches. The ridge orientations are random and do not correspond to intersections between the {111} slip planes and the {111} surface. The most likely explanation is that early polishing stages introduced substantial compressive residual stresses that are "locked in" by dislocation structures. The annealing removes these dislocations and the stress relief is accompanied by projection of the previously compressed material above the sample surface. These ridges are removed by electropolishing the sample surface for 90 s at a constant current density of 1 A/cm^2 using a electropolishing solution of 37 % phosphoric acid, 56 % glycerol, and 7 % water, by volume. This final step produces an optically perfect surface, although measurements show residual broad features with maximum heights of around 20 nm to 30 nm. These features can be avoided by using AFM to locate flat regions suitable for nanoindentation.

Future work will use sub-micrometer, depth-resolved diffraction (Levine et al., 2006; Levine et al., 2011) at sector 34 of the Advanced Photon Source at Argonne National Laboratory to characterize the local dislocation density, residual elastic strain tensor, and crystallographic orientation throughout the volume beneath the touchdown point, both before and after nanoindentation. Such characterization can both verify the suitability of the target location and provide a quantitative measure of the microstructural changes and residual stresses that result from a nanoindentation measurement.

2.4.3. Nanoindentation experiment

In addition to having detailed knowledge of indenter tip shape and initial sample conditions, accurate experimental determination of properties such as initial plastic yield stress and elastic moduli also requires that the instrumented nanoindentation instrument produces accurate load and displacement data. As will be shown below, the measurement ranges of interest for studying the onset of plastic yield are typically below 1 mN for applied force (load) and below 20 nm for the displacement of the indenter tip into the specimen surface. If the accuracy in mechanical properties calculated from force and displacement data is desired at the level of a few percent, then both force and displacement data must be accurate to approximately 1 % in these ranges; this is a challenging task.

In the calibration of force, the two greatest challenges are obtaining accurate reference forces and transferring those reference forces to the nanoindentation instrument. Recently, however, techniques have been developed to realize forces down to 10 nN that are traceable to the International System of Units (SI) through the use of electrostatic forces, and those forces can be transferred traceably to nanoindentation instruments with the same level of accuracy using transfer force cells (Pratt et al., 2005) that can be placed directly in the instrument, in place of a specimen.

The problem of measuring indentation depth poses a different set of problems. In principle, length metrology with the necessary level of accuracy is easily available through the use of laser interferometer systems (see, for example, Smith et al., 2009). However, the indenter penetration depth, *h,* is necessarily defined as the depth to which the indenter penetrates the original plane of the specimen surface. This, however, is not the displacement that many commercial nanoindentation instruments measure; very often, they measure the motion of the indenter tip and the shaft to which it is mounted relative to housing (often referred to as a "load head") that contains the indenter shaft. In this arrangement, the compliance of the load frame – the mechanical path between the load head and the specimen – becomes a direct source of error in determining *h* from the measured displacement (Oliver & Pharr, 1992). Future work will include the design, construction and use of a nanoindention instrument capable of non-contact sensing of the location of the specimen surface, allowing a more direct measurement of penetration depth. This instrument will provide an SI-traceable path for force calibration as well.

3. Combined experimental and modeling method

In this section, we introduce our combined experimental and finite element analysis (FEA) method to study the effect of spherical indenter tip assumption on the initial plastic yield stress of <100>-oriented single crystal tungsten from nanoindentation.

3.1. Indenter tip shape measurement

The near-apex shape of two real diamond Berkovich indenters, one lightly and another heavily used, were measured using an Asylum Research MFP-3D[1] (Santa Barbara, CA) AFM in intermittent contact mode. This instrument uses a two-dimensional flexure stage under closed-loop control with position measurement by linear variable differential transformers (LVDTs). Motion of the stage is therefore decoupled from the vertical motion of the scanner, eliminating cross-coupling artifacts found in tube-type scanners. The vertical motion is also under closed-loop control with displacement measured by LVDT.

The Berkovich probes were cleaned using carbon-dioxide "snow" (Morris 2009). Silicon cantilevers with tip radii of 5 nm to 10 nm and approximately 300 kHz bending resonance

---

[1] Certain commercial equipment, instruments, software, or materials are identified in this paper to foster understanding. Such identification does not imply recommendation or endorsement by the National Institute of Standards and Technology, nor does it imply that the materials or equipment identified are necessarily the best available for the purpose.

frequencies were used to image the indenters. The AFM images were taken at a resolution of 256 x 256 pixels in a 1.25 µm × 1.25 µm region. A sharp silicon-spike tip characterizer (TGT-1, NT-MDT, Moscow, Russia) was scanned before and after imaging to verify that there were no double-tip artifacts or other deformities. Four hours were allowed before the final shape measurement to allow the temperature to stabilize within ± 0.1 °C. Drift-rate characterization experiments utilizing image correlation software showed that this reduced thermal expansion/contraction drift to less than 0.5 nm min^{-1}.

3.2. Nanoindentation experiment

The nanoindentation experiments were previously described in Li, et al. (2012). Cylindrical tungsten crystals were prepared by first grinding to SiC 600 grit. Grinding damage at the surface was then removed by electropolishing for several minutes at 20 V in a solution of 50 % glycerol (by volume) and 50 % water with 1.25×10^{-3} mol m^{-3} NaOH (Vander Voort, 1984; Zbib & Bahr, 2007). Electropolished tungsten at room temperature has a negligible (sub-nanometer thick) oxide present (Bahr et al., 1998).

The indentations on the electropolished tungsten were performed with a Hysitron (Minneapolis, MN) Tribo-Scope attachment to a Park (Santa Clara, CA) Autoprobe CP scanning probe microscope in ambient laboratory conditions. For the lightly used indenter, the loading schedule was as follows: loading to 100 µN, a partial unloading to 80 µN, then final loading to 700 µN at rates of 20 µN s^{-1}. The indenter was held at the peak load for 5 s, then unloaded to 140 µN at 60 µN s^{-1}. The purpose of the initial load-unload sequence was to inspect for plastic deformation prior to the first pop-in event. If the load-displacement data were different prior to the first pop-in event, then the elastic analysis was not used.

3.3. Finite element modeling

The commercial FEA package, Abaqus (Abaqus, 2011), was used for modeling the nanoindentation of a single-crystal tungsten sample. To accurately simulate nanoindentation in the elastic regime, the two AFM-measured indenter shapes were directly input into FEA models (Ma & Levine, 2007; Ma et al., 2009, 2012). First, high-frequency measurement noise in the AFM data was removed through a combination of median and averaging filters. No change in the orientation of the image was made (as would occur if the image were plane-fitted and leveled). After filtering, the discrete AFM data were interpolated to a 2.44 nm spacing using bi-cubic interpolation. Next, since W is a very stiff material, the AFM-measured indenter tip shapes were meshed with three dimensional (3D) deformable elements with a flat rigid plate at the top. A 2D elastic-deformation parameter study was carried out to determine the distance from the rigid plate to the 3D deformable indenter tip that was needed to avoid introducing artifacts into the nanoindentation simulations. In addition, complementary simulations of indentation by parabolic probes took advantage of the full symmetry of a sphere and four-fold

symmetry of {100} W, so only one quarter of a sphere and specimen were modeled to reduce the computational burden. In all cases, contact between the indenter and specimen was assumed to be frictionless.

For the details of the FEA specimen mesh for both indenters, please see (Ma et al., 2009, 2012). The complete tungsten specimen and diamond indenter mesh was created using eight-node reduced-integration linear brick elements. In the contact region, the FEA mesh is high-density. The diamond element length is 2.44 nm. For the tungsten specimen, each element has a length of 1.266 nm (4 unit cells across) with nodes aligned to tungsten atom positions. This will facilitate future atomistic simulations that use the under-load state as a boundary condition (Wagner et al., 2008). Constitutive behavior was linear elastic, and fully anisotropic for the tungsten and isotropic for the diamond. Expressed using the crystallographic body-centered cubic (BCC) basis vectors, each edge of the tungsten mesh elements is <100>. The stiffnesses of tungsten are C_{11} = 522 GPa, C_{12} = 204 GPa, and C_{44} = 161 GPa (Lide, 2007); For the diamond indenter, the Young's modulus is selected from the published indentation modulus of {100} diamond (1126 GPa) and Poisson's ratio is 0.07 (Vlassak et al., 2003).

4. Results and discussion

4.1. Indenter tip shape

Figures 2(a) and 2(b) are the AFM rendering images of the lightly- and heavily-used Berkovich indenters, respectively. Figures 2(c) and 2(d) are the corresponding contour plots of the near-apex region with 2 nm contour spacing after interpolation and filtering, as described in Sec. 3.3. Note that the contour plots for both indenters are plotted to the same scale. It can be seen that the lightly-used indenter is much sharper while the heavily-used indenter is flattened and blunt in the near-apex region, as expected. From the data shown in Figs. 2(c) and 2(d), the radius of curvature at the apex may be estimated, although not in a unique way. It is difficult to assign a unique "radius of curvature" to a point on a general 3D object (Bei et al., 2005; Constantinides et al., 2007; Ma et al., 2009; Tyulyukovskiy & Huber, 2007). Constantinides, et al. (2007) approached this problem when characterizing conospherical diamond probes by fitting osculating paraboloids to sub-areas within the AFM images, and assigning a local radius to the pixel located at the vertex of the paraboloid. Tyulyukovskiy & Huber (2007) characterized AFM-measured shapes of spherically machined diamond probes by fitting the projected-area function to an equation that described a sphere with increasing imperfection closest to the apex. In the current study, the radius of curvature was estimated by fitting parabolas to several evenly spaced profiles through the apex (Ma et al., 2009). The mean radius estimated by this method is 121 nm ± 13 nm for the lightly-used indenter tip and 1150 nm ± 14 nm for the heavily-used indenter tip. All measurement uncertainties in this chapter are one standard deviation.
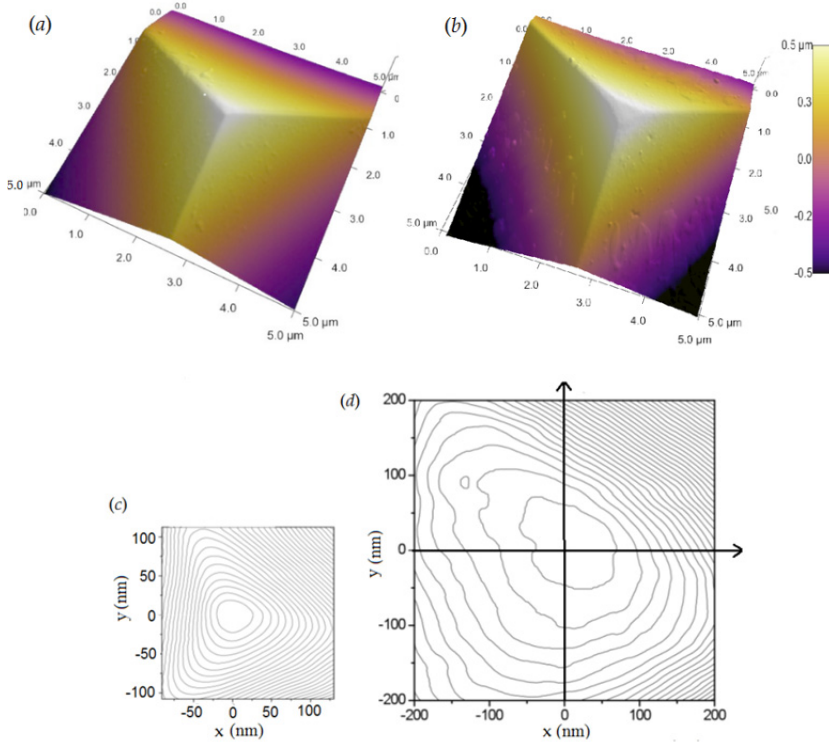
Figure 2. Three-dimensional AFM rendering image of the lightly (a) and heavily (b) used indenters, and contour plot of the surface of the lightly (c) and heavily (d) used indenter shape in the near-apex region with 2 nm contour spacing after interpolation and filtering.

4.2. Nanoindentation experiments

The AFM-measured sharp and blunt Berkovich probes were used to perform load-controlled nanoindentation experiments on the same <100>-oriented single-crystal tungsten specimen. For both indenters, ten indentation tests were performed as described in Sec. 3.2. All indentations exhibited a significant first pop-in event, but only six indentations using the sharp indenter and five indentations using the blunt indenter showed no plastic deformation during the initial unloading-reloading sequence, as described above. These are the only indentation tests that were analyzed further. Figure 3 shows load versus displacement data for two representative indentation experiments on tungsten, one using the sharp indenter and the other using the blunt indenter. In both sets of data, the nucleation event is seen clearly at the critical load, P_{CRIT}. The indenter radius was estimated by a least-squares fit of the Hertzian relationship to data preceding P_{CRIT},

$$P = \frac{4}{3}\bar{E}_R R^{1/2}\left(h - h_{OFF}\right)^{3/2}, \tag{3}$$

where an additional offset displacement, h_{OFF}, is used to adjust for uncertainty in the point of first contact. A reduced elastic indentation modulus of $\bar{E}_R = 317\ \text{GPa}$, found from the published indentation modulus of {100} diamond (Vlassak et al., 2003) and the stiffness coefficients of tungsten listed in Section 3.3 (for $\bar{E}_W = 442\ \text{GPa}$), was used to estimate R. Offset displacements found from fitting were less than 1 nm for both indentation experiments. Averaging over all of the accepted indentation tests, the mean radii are 163 nm ± 13 nm for the sharp indenter and 1160 nm ± 22 nm for the blunt indenter. This radius for the sharp indenter is significantly larger (≈ 35 %) than that inferred from the AFM measurement, while those for the blunt indenter are in good agreement.
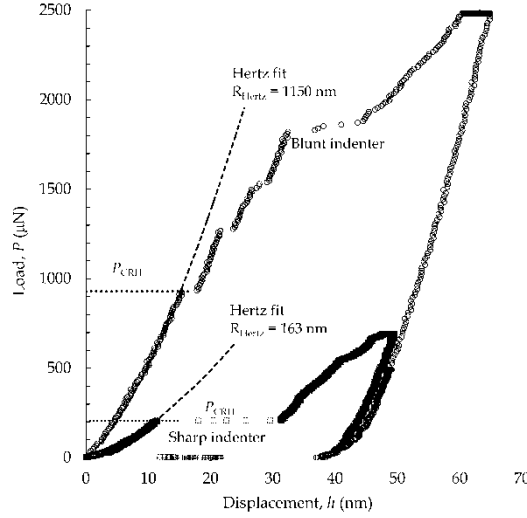

Figure 3. Load as a function of displacement for two representative indentation experiments on tungsten, one using the sharp indenter and the other using the blunt indenter. The critical load for plastic deformation, P_{CRIT}, is shown on each. A Hertzian fit to the initial elastic loading portion is drawn. The statistical uncertainty in P_{CRIT} is described in the text.

From the average indentation load at the first pop-in event (P_{CRIT} = 233 µN ± 90 µN for the sharp indenter and P_{CRIT} = 851 µN ± 131 µN for the blunt indenter) and the radius of the probe as inferred from fits to Eq. 3, the maximum shear stress, τ_{MAX}, may be estimated from Eq. 2, which assumes an isotropic material with Poisson's ratio equal to 0.3. The test-by-test average τ_{MAX}, estimated at the displacement excursion, was τ_{MAX} = 16.5 GPa ± 1.6 GPa for the sharp indenter and 7.1 GPa ± 0.4 GPa for the blunt indenter. The τ_{MAX} for the sharp indenter agrees with our earlier nucleation shear stress estimates on W using a rigid indenter simulation with a scaled modulus (Ma et al., 2009; Zbib & Bahr, 2007; Bahr et al., 1998). The τ_{MAX} obtained using the blunt indenter is much smaller, only about 43 % of that from the sharp indenter. This difference in τ_{MAX} is consistent with nanoindentation size effects reported by other researchers (Morris et al., 2004; Shim et al., 2008). In those studies, the maximum shear stress under small spherical indenters at the first pop-in was found to be very high, on the order of the theoretical strength; for larger spheres, the maximum stress decreased with increasing indenter radius.

The most likely explanation for this observed behavior is that the number of dislocations in the stressed volume increases with indenter radius. Thus, for sufficiently small indenters, the material in the highly stressed zone underneath the indenter is likely to be dislocation-free, requiring dislocation nucleation at the theoretical stress. As the indenter radius increases, there is an increasing likelihood that a nearby dislocation assists in the onset of plasticity. When a sufficiently large volume of material is probed, plasticity tends to be initiated by the motion of preexisting dislocations rather than by the nucleation of new dislocations.

Mason et al. (2006) and Schuh and Lund (2004) have suggested that pop-in events should have a rate-dependence wherein higher loading rates will generally correspond to higher pop-in loads. To examine this we have carried out a series of indentations into a model BCC system [Fe-3%Si by weight single crystal in the (100) orientation] using a Berkovich indenter similar to that shown in the remainder of this study. The indentations were made in the same Hysitron Triboindenter system, and regions of the sample were examined using scanning probe imaging prior to indentation. Between 50 and 100 indentations were made at loading rates of 5, 50, and 100 mN/s, and all samples that exhibited solely elastic loading prior to yield were selected. The cumulative probability of yield, as described by Schuh and Lund (2006), was used to determine the effect of loading rate on yield behavior. As shown in Fig. 4, there is no statistically significant effect of the load (and therefore stress) at yield due to indentation rate over the range tested. The experimentally observed results are similar to the results by Rajulapati et al. (2010), Wang et al. (2011), and Vadalakonda et al. (2006) in that the onset of plasticity is not significantly impacted by the loading rate for Ta (bcc), Mo (bcc), and Ni (fcc) single crystals, and polycrystalline W, Fe, and Ni. This suggests that the rate dependence observed by Mason et al. (2006) and Schuh and Lund (2004) in Pt may imply there are multiple processes that control the onset of plastic deformation, and that loading rate may impact some, but not all, of these processes.
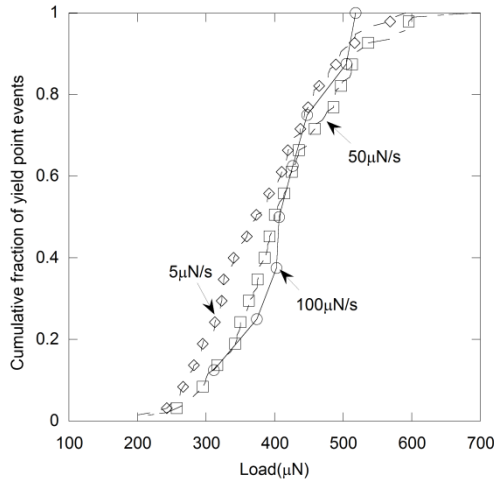

Figure 4. Rate dependence on yield behavior in Fe-3%Si sample. No effect of loading rate is noted in this material for these rates, the cumulative fraction of yield points as a function of load at which the yield point occurs is indistinguishable over these loading rates.

4.3. Comparison of FEA results to experiment

In general, directly modeling an indentation experiment using the FEA should produce a more accurate estimate of the indentation stresses than the simple Hertz approximation. However, it should be understood that there are computational difficulties with 3D FEA which prohibit a completely faithful virtual representation of the experiment and the computational times must be kept manageable. Generally, the indenter is kept rigid to avoid a full interior meshing and consequent increase in simulation size. This is not a problem when simulating the indentation of materials that are much more compliant than diamond; however, the stiffness of tungsten is an appreciable fraction of that for diamond. Nevertheless, our earlier work on a sharp indenter showed that a simulation using a rigid indenter matched the experimental results extremely well when these results were scaled using the "effective modulus" (Ma et al., 2009).

Since tungsten is very stiff, the high loads encountered during indentation can produce appreciable elastic deformation of the indenter tip, and it is necessary to quantify these changes and determine their effect on the nanoindentation experiment. Fortunately, the advent of highly-parallel computer architectures has made it possible to complete large 3D FEA models within manageable computational time. In this research, both AFM-measured indenters were input into FEA models with 3D deformable elements as described in sec 3.3. All of the displacement measurements in the FEA simulations are measured with respect to the reference point of the indenter rigid plate (just like the experimental measurements) unless otherwise specified.

Figures 5 and 6 show the measured load-displacement curves for all of the analyzed indentation experiments using the sharp and blunt indenters, respectively. The first contact points in the experimental data were adjusted slightly as described in sec 4.2 and the dotted lines indicate the major pop-in location for each experiment. The FEA-simulated elastic deformation curves (with deformable AFM-measured Berkovich indenters) are plotted for comparison. The simulated load-displacement curves and all of the experimental plots were in good agreement with each other for both the sharp and blunt indenters. The deviation between some of the measured and simulated curves in Fig. 6 at large indentation depth (above 12 nm) is caused by small amounts of plastic deformation. In some cases, this occurred slightly before the major pop-in events which are the main emphasis in this paper.

The FEA-simulated Berkovich load-displacement data for both the sharp and blunt indenters are replotted in Fig. 7. These data may be analyzed as if they came from a physical measurement, and Hertzian fits (using Eq. 3) to these data are shown as smooth curves. The resulting Hertzian-estimated radii are 163 nm for the sharp indenter and 1160 nm for the blunt indenter. These radii were then used for additional FEA simulations using deformable parabolic indenters (designated FEA_Hertz simulations) and the results are shown as black open circles for the blunt indenter and black open diamonds for the sharp indenter. All of the load displacement curves are in good agreement for the blunt indenter as shown in Fig. 7. However, the FEA_Hertz simulation for the sharp indenter exhibited a stiffer contact than that predicted from the Hertz equation; by trial and error, an FEA_HERTZ simulation using

a radius of 125 nm (plotted using open squares in Fig. 7) was found to match the simulated Berkovich *P-h* relationship very well. A similar discrepancy between a rigid-sphere FEA simulation and the Hertz solution was described previously (Ma et al., 2009).
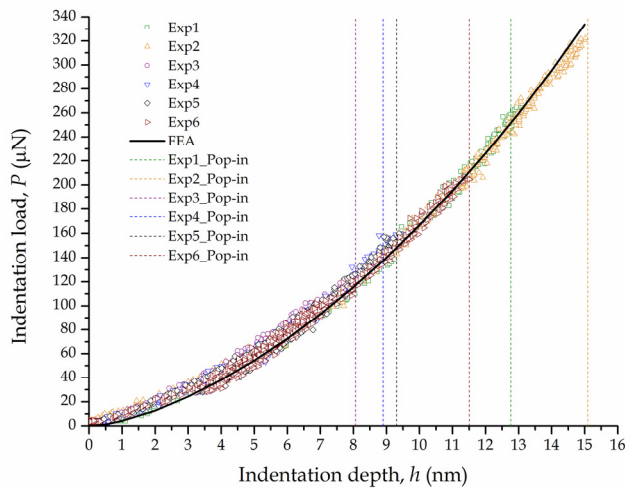

Figure 5. Measured load-displacement curves for all analyzed indentation experiments using the sharp indenter and the corresponding FEA-simulated elastic deformation curves using the AFM-measured indenter. The dotted lines indicate the major pop-in location for each experiment.
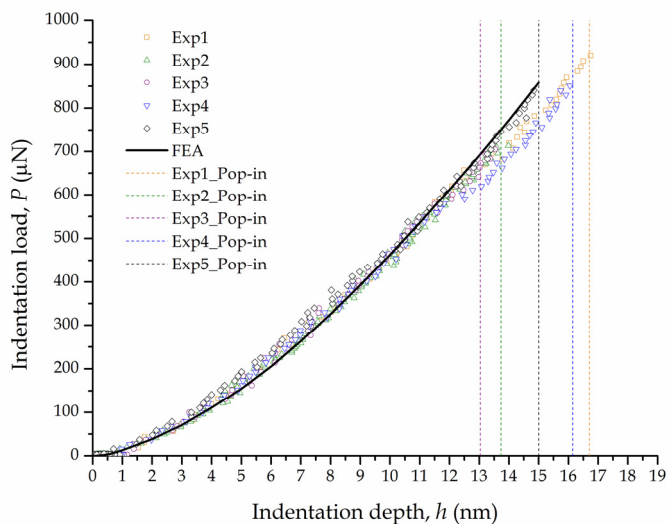

Figure 6. Measured load-displacement curves for all analyzed indentation experiments using the blunt indenter and the corresponding FEA-simulated elastic deformation curves using the AFM-measured indenter. The dotted lines indicate the major pop-in location for each experiment.
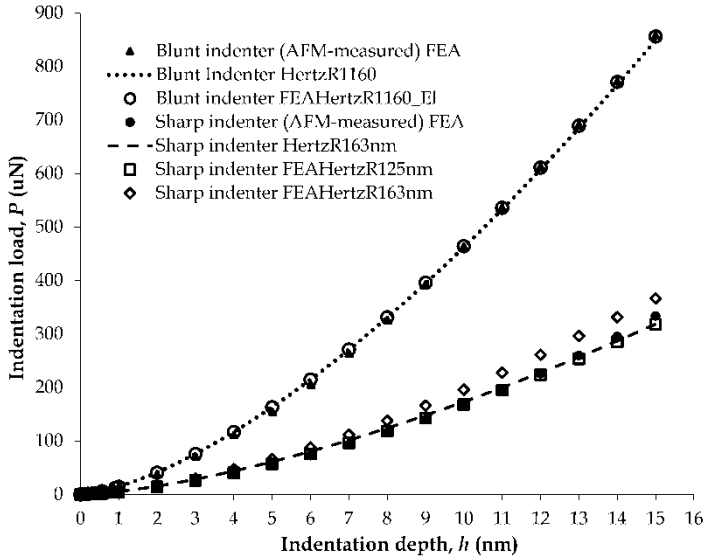
Figure 7. All of the FEA-simulated and Hertzian load-displacement curves for both the sharp and blunt indenters.

Figures 5 and 6 demonstrate that the simulated load-displacement relationships for the Berkovich-probe indentation agree with the experimental indentation results, and Fig. 7 shows that the analytic Hertz approximation and simulations using a deformable parabolic indenter can produce comparable load-displacement results. The next step is to compare the resulting simulated Tresca stresses, which is defined as the maximum difference between principal shear, throughout the specimen for all of these analysis methods.

Table 1 lists the radii and maximum shear stresses derived from the experimental data and the FEA simulations for both the sharp and blunt indenters. Figures 8a and 8b show the contact-surface shear-stress contours for the sharp indenter (Fig. 8a) at an indentation depth of 11 nm, and the blunt indenter (Fig. 8b) at an indentation depth of 15 nm, from the FEA simulations using the 3D deformable Berkovich indenter. These depths correspond to the average indentation depths where pop-ins occurred in the experiments. The contours show the shapes of the indenter tips at small scale. Figures 8c and 8d are the corresponding perspective views that show the distributions of shear stress around the locations of maximum shear stress ($\tau_{Tr}/2$). The stress contours are set so that shear stresses larger than those predicted by the Hertz approximation are shown in grey. Thus, the grey-region for the sharp indenter in Fig. 8c has $\tau_{Tr}/2 \geq 16.3$ GPa; for the blunt indenter in Fig 8d, this limit is $\tau_{Tr}/2 \geq 7.1$ GPa.

The shear-stress contours for both Berkovich probes in Fig. 8 exhibit pronounced irregularities that correspond to the non-spherical probe shape. For the sharp indenter (see Figs. 8a and 8c), the average indentation depth for the first pop-in is deep enough so that the

three-sided pyramid region affects the shapes of the stress contours. Also, the innermost contour (gray color in Fig. 8c) encompasses a large volume where the shear stress exceeds the Hertzian estimate for the same indentation load and depth. Finally, although the point of maximum shear stress is located below the sample surface, in agreement with Hertz contact theory, it is shifted slightly from the central axis and towards the surface. For the blunt indenter (see Fig. 8b and 8d), the stress contours do not exhibit a clear three-sided shape such as that seen from the sharp indenter. However, the pattern of high shear stress within the sample is extremely irregular and is strongly influenced by the irregular shape of the indenter. The sample volumes where the shear stress exceeds the Hertzian estimate (gray color in Fig. 8d) are concentrated in several small local regions directly underneath the contact surface. Thus, the irregular shape of the measured indenter produces numerous volumes of highly localized shear stress that are higher than those produced by a spherical probe with an indistinguishable load-displacement relationship. In addition, the locations of these highly-stressed regions are not generally on the indentation axis and they occur much closer to the sample surface than predicted by the Hertz theory.

	Sharp Indenter	Blunt Indenter
Hertzian radius (nm)	163 ± 13	1160 ± 22
AFM measured radius (nm)	121 ± 13	1150 ± 14
FEA simulated radius (nm)	125	1160
Average depth for 1st pop-in (nm)	11	15
Load at average pop-in depth (μN)	233 ± 90	851 ± 131
τ_{MAX} (Hertz-estimated) (GPa)	16.3 ± 1.6	7.1 ± 0.4
	$\approx G/10$	$\approx G/20$
τ_{MAX} (FEA) (GPa)	23.0 ± 2.0	14.0 ± 0.5
	$\approx G/7$	$\approx G/12$

Table 1. Lists the radii and maximum shear stress derived from the experiment and FEA simulation for both the sharp and blunt indenters.

Figure 9a plots the maximum shear stress in the sample as a function of indentation load for the 3D Berkovich FEA simulations, the Hertz predictions, and the FEA Hertz simulation for the sharp and blunt indenters. Figure 9b plots the percent deviation of the Hertzian and FEA Hertz predictions from the more rigorous 3D Berkovich FEA simulations. It can be seen that the maximum shear stress from all of the Hertzian and FEA Hertz estimates are much smaller than those found from direct FEA simulation of the real indenter probe.

For the sharp indenter, all of the shear stress curves exhibit a smooth increase with increasing indentation load, consistent with the generally smooth character of the indenter tip shape. However, the FEA Hertz result deviates from the 3D Berkovich simulation by about 5 % to 8 % at the experimentally found pop-in load of P_{CRIT} = 233 μN ± 90 μN. At smaller loads, this deviation is even greater, increasing to around 20 % at an indentation load of about 6 μN. Meanwhile, the Hertzian estimate of the radius (R=163 nm) from the experimental data is much larger than those obtained from the direct AFM measurement (R = 121 nm ± 13 nm) and FEA Hertz fitting of the experimental load displacement curves (R =

125 nm). This overestimation of the sharp indenter tip radius introduces a substantial bias to the Hertz estimate of the maximum shear stress. The maximum shear stress is underestimated by more than 25 % at the pop-in loads and increases to more than 30 % at lower loads.
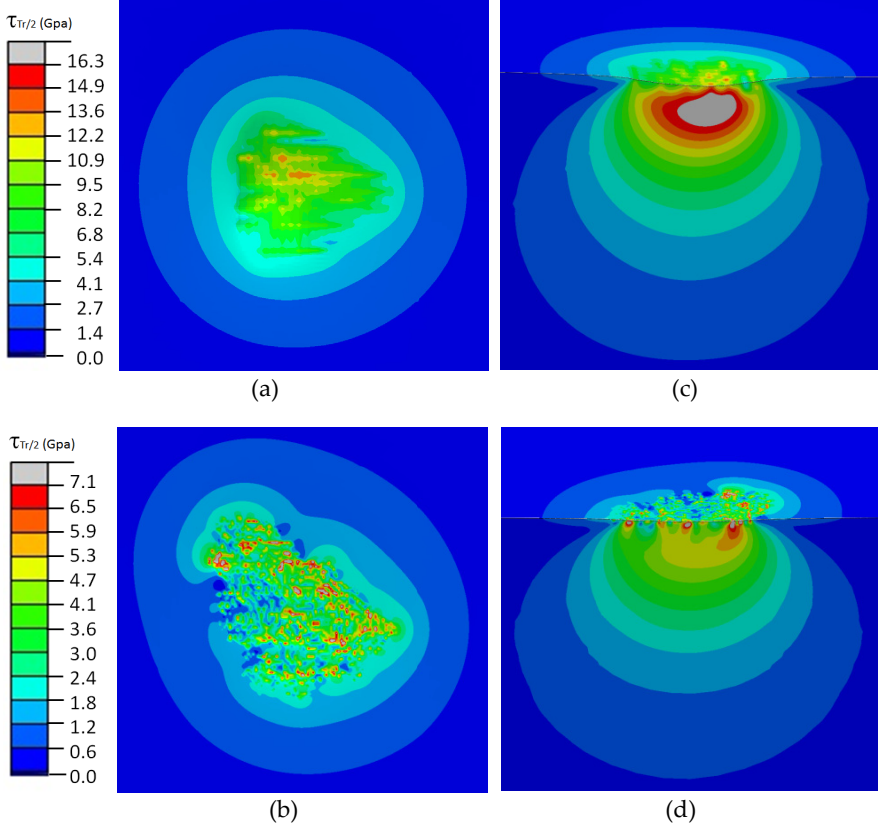

Figure 8. FEA Contact surface shear stress contours for both the sharp (a) and blunt (b) indenters and their perspective views ((c) sharp and (d) blunt indenters). The indentation depths were 11 nm for the sharp indenter and 15 nm for the blunt indenter.

For the blunt indenter, the tip radii obtained from the AFM measurement, the Hertzian estimate and the FEA Hertz simulation are all in good agreement (see Table 1). Thus, it is not surprising that the maximum shear stresses predicted by the Hertz approximation and the FEA Hertz simulation are nearly identical, as shown Fig. 9. However, the irregularity of the real indenter tip shape produces large stress excursions away from the more macroscopic stress contours. Thus, the Hertzian approximation and the FEA Hertz simulation both underestimate the maximum shear stress by more than 50 % at the pop-in loads (P_{CRIT} = 851 µN ± 131 µN) and this error increases to more than 70 % at smaller loads. This deviation is much larger than that found for the sharp indenter.
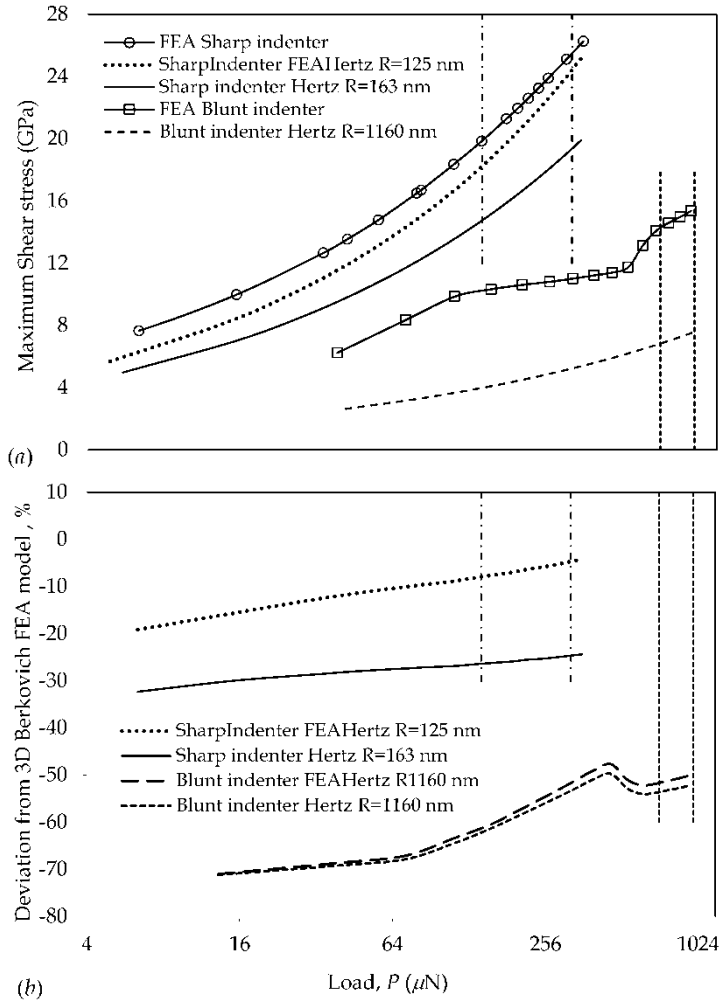
Figure 9. a) The maximum shear stress in the sample as a function of indentation load for the 3D Berkovich FEA simulations, the Hertz predictions, and the FEA Hertz simulations for the sharp and blunt indenters. B) The corresponding percent deviation of the Hertzian and FEA Hertzian predictions from the more rigorous 3D Berkovich FEA simulations.

The obvious irregularity of the blunt indenter is reflected in the distribution of maximum shear stresses within the sample (see Fig. 8b and 8d) and the behavior of τ_{MAX} with increasing indentation load (see Fig. 9). In Fig. 9a, the maximum shear stress under the blunt 3D Berkovich indenter (square with line) shows a distinct two step behavior. Thus, the stress increases fairly rapidly up to an indentation load of about 110 µN (about 4 nm indentation depth) where it abruptly slows. At an indentation load of about 538 µN (about 11 nm indentation depth) τ_{MAX} again increases rapidly with a tapering slope.

Figure 10 shows two perpendicular cross-section profiles (passing through the apex) of the 3D AFM-measured blunt indenter as shown in Fig. 2d. These cross sections show pronounced changes in curvature at a variety of distances from the apex. It is probable that such local shape changes are largely responsible for the irregular behavior of the blunt 3D Berkovitch τ_{MAX}-load plot.
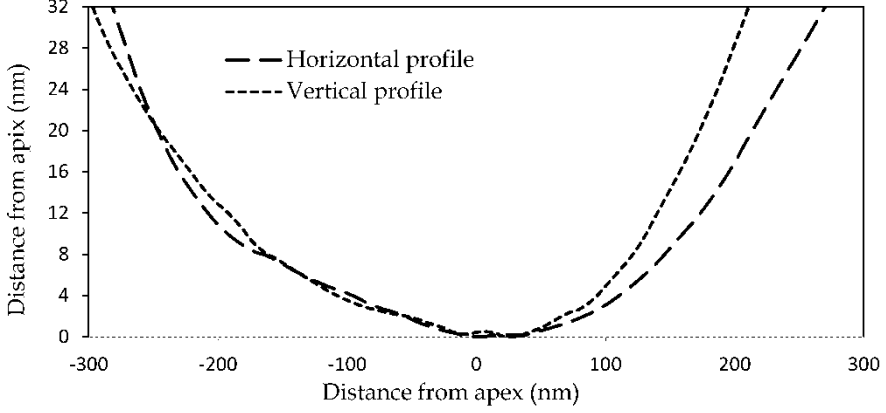

Figure 10. Two perpendicular cross-section profiles (passing through the apex) of the 3D AFM-measured blunt indenter as shown in Fig. 2d.

As shown in Fig. 2, new diamond Berkovich indenters have a faceted-pyramid shape with an approximately spherical end cap. Theoretically, the transition from the spherical cap to the pyramid geometry can be approximated using a simple geometrical model, where the spherical region is tangentially enclosed within an open-cap conical geometry, giving:

$$h^*/R = 1 - \sin\theta, \tag{4}$$

where h^* is the transition depth and θ is the semi-angle of the conical part (Cheng & Cheng, 1998; VanLandingham et al., 2005; Constantinides et al., 2007). For an axisymmetric approximation of a Berkovich probe, $\theta = 70.3°$ and $h^* = 0.0585\ R$. Thus, the sharp indenter with $R = 125$ nm has a predicted transition at $h^* = 7.3$ nm, which is smaller than any of the measured pop-in depths and explains the pronounced 3-fold symmetry of the surface-stress contours in Fig. 8a. The predicted transition for the blunt indenter with $R = 1160$ nm is considerably larger at $h^* = 67.86$ nm. In reality, after frequent indention, the diamond indenter tip will be worn on the apex (see Fig. 2), decreasing the transition depth. Nevertheless, a transition to the pyramidal region was not observed for the blunt indenter.

The approximate sphere-cone load-displacement relationship also follows a generalized power-law relationship,

$$P = Ch^m, \tag{5}$$

where C and m are constants. If fitted to Eq. 5, the P-h relationships from the 3D Berkovitch simulations have a best-fit parameter of $m = 1.59$ for the sharp indenter and $m = 1.54$ for the blunt indenter. Because $m = 1.5$ (Hertz) for a sphere, and $m = 2$ for a cone, an intermediate m is generally interpreted to mean that the spherical and conical parts of the indenter were both in contact with the material at the point of pop-in. This is certainly true for the sharp indenter as described above.

Next the contact radius, a, was estimated by the Hertzian relationship (Johnson, 1999),

$$a = \left[\frac{3PR}{4\overline{E}_R} \right]^{\frac{1}{3}}$$

(6)

Johnson (1999) observed that "… doubt must be cast on the Hertz results if the ratio a/R becomes too large. With metallic bodies, this restriction is ensured by the small strains at which the elastic limit is reached…". Yoffe (1984) shows that the surface displacement field, including the effect of lateral displacements in the contacted zone, for a Hertizan contact begins to deviate significantly from that of a sphere at normalized contact radius $a/R \approx 0.2$ when the Poisson's ratio of the indented material is $v \approx 0.3$. The normalized contact radius at the average pop-in position for the blunt indenter is about $a/R \approx 0.11$ for the estimated radius of 1160 mm. However, the sharp indenter shows roughly $a/R \approx 0.25$ for the Hertz estimated radius of 163 mm and $a/R \approx 0.34$ for the AFM measured radius $R = 121$ nm. This significantly exceeds Yoffe's rue for the limits of Hertizian theory (Li et al., 2009).

Finally, it is well known that diamond indenters will exhibit substantial elastic deformation when indenting materials like tungsten that have an appreciable fraction of the diamond stiffness. This elastic deformation can be quantified by subtracting the displacement of the indenter tip from the displacement of the indenter base, here referred to as the elastic depth difference. Since almost all of the indenter deformation occurs near the tip where the cross-sectional area is small, the elastic depth difference is a well-defined quantity as long as the simulated base is far enough away from the tip as described in section 3.3. Figure 11 shows the elastic depth difference plotted as a function of indentation load for the 3D Berkovich FEA simulations and the FEA Hertz simulations for both the sharp and blunt indenters. At a given indentation load, the sharp indenter deforms the most because of its smaller cross section. This difference between the sharp and blunt indenters increases nonlinearly with the indentation force. The 3D Berkovich indenters deform more than the parabolic FEA Hertz indenters, but this difference is very small.

The amount of elastic deformation exhibited by the sharp indenter in Fig. 10 is an appreciable fraction of the total indentation depth. For example, the average pop-in depth for the sharp indenter was about 11 nm, with a corresponding load of about 196 μN. At this load, the elastic deformation depth from Fig. 11 is almost 3.7 nm, demonstrating that the shape of the indenter is being severely modified by the elastic stresses.
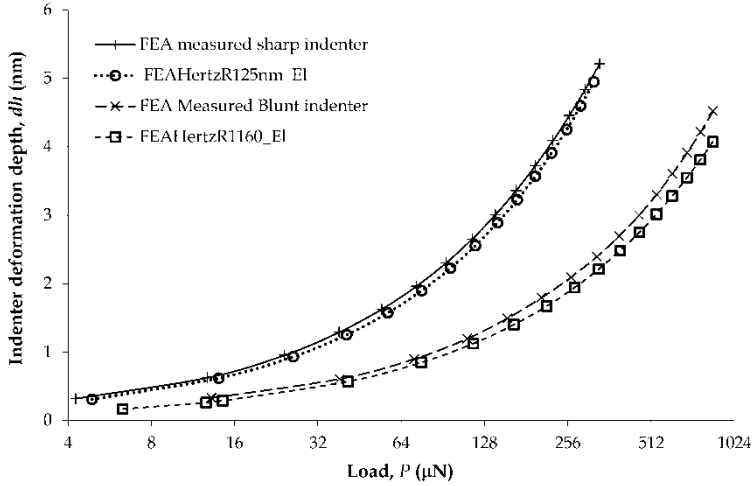
Figure 11. The elastic depth difference as a function of indentation load for the 3D Berkovich FEA simulations and the FEA Hertz simulations for both the sharp and blunt indenters.

5. Conclusion

Hertzian elastic contact theory is broadly used by the nanoindentation community to estimate the stresses required for interesting events such as pop-ins. However, the Hertzian approximation makes a number of assumptions that may not be valid for real systems; these include assumptions concerning the sphericity of the indenter tip, the flatness of the specimen, and a low ratio of indentation contact radius to indenter tip radius. In real systems, the indenter tip can be markedly irregular at nanometer length scales, the sample surface can have an irregular shape, and the indentation depth for the first pop-in can be deep enough so that the non-spherical sides of the indenter can contact the specimen. Additional problems that can occur include quantitative calibration of the nanonewton-level loads and determination of the actual indentation depth and contact area.

In this review chapter, we described some of the challenges and limitations for extracting the initial plastic yield stress from nanoindentation with the spherical indenter tip assumption, and we assessed possible errors and pitfalls of the Hertzian estimation of initial plastic yield at the nanoscale. Ultimately, solving these problems will require the development of new standard test methods and standard reference materials and this chapter describes some of our going work at NIST in that direction, including 1) measurements of the sample and indenter tip shapes using an AFM system that uses laser interferometry (traceable to NIST primary reference standards) for all distance measurements, 2) development of a custom nanoindentation instrument for nanoindentation where load and displacement are again traceable to primary NIST reference standards, 3) 3D, submicrometer resolution, synchrotron X-ray measurements of the local elastic strain tensor, crystallographic orientations, and dislocation density

throughout of indentation volume both before and after indentation, and 4) combined FEA and molecular dynamics modeling of the experiments using the experimental measurement as direct inputs.

A preliminary combined experimental and FEA study was described where <100>-oriented single-crystal tungsten was used to examine the role of the indenter tip shape on nanoindentation determinations of the maximum shear stress at the dislocation nucleation point (plastic yield stress). The near-apex shape of two real Berkovich indenters, one slightly and another heavily used, were measured using AFM. These shapes were then used as a "virtual" indentation probe in a 3D FEA simulation of nanoindentation experiments on <100>-oriented single crystal tungsten. Independently, instrumented nanoindentation experiments were carried out with the real indenters on <100>-oriented single crystal tungsten. The agreement between the FEA and experimental load-displacement curves was excellent, and the FEA simulations provide a validated point-of-comparison for more conventional model predictions.

Analytic Hertzian fits and FEA simulated Hertzian simulations were also carried out, and the resulting fits to the load displacement data were excellent, even though there were substantial deviations from a spherical or parabolic geometry. These results demonstrate that even a highly irregular probe will produce an elastic load-displacement relationship that could be perceived as having originated from a spherical contact. That is, although the load-displacement data could reasonably be described by a fit using the Hertzian relationship, the contacting surfaces certainly did not fit the Hertzian criteria (specifically, that of contacting paraboloids) and the fitted radius for the small indenter was off by 35 %. Not surprisingly, the simulations showed that the irregular probes generated shear stresses in the sample that were significantly different, both in magnitude and location, from those generated with a true spherical probe. The effect of asphericity and other irregularities were dominant, focusing the indentation force into a smaller volume, and thereby increasing the maximum shear stress in the body over that produced by an ideal spherical contact. Hertzian estimates of the maximum shear stress in tungsten at the pop-in loads were smaller than those determined from FEA by over 25 % for the lightly used indenter and over 50 % for the heavily used indenter.

Author details

Li Ma, Lyle Levine, Ron Dixson and Douglas Smith
National Institute of Standards and Technology, USA

David Bahr
Washington State University, USA

Acknowledgement

6. References

Abaqus/Standard (2011). *Theory and User's Manual,Version 11.1* , Dassault Systemes Simulia

Aldrich-Smith, G.; Jennett, N. M. & Hangen, U. (2005). Direct Measurement of Nanoindentation Area Sunction by Setrological AFM, *Z. Metallkd.* Vol. 96, No. 11, pp. 1267-1271, ISSN 0044-3093

Bahr, D. F.; Kramer, D. E. & Gerberich, W. W. (1998). Non-linear Deformation Mechanisms During Nanoindentation, *Acta Materialia*, Vol. 46, No. 10, pp. 3605-3617, ISSN 1359-6454

Bei, H., George, E.P., Hay, J.L., Pharr, G.M., 2005. Influence of Indenter Tip Geometry on Elastic Deformation During Nanoindentation, *Physics Review Letters*, Vol. 95, pp. 045501-045501-4

Bradby, J. E. & Williams, J. S. (2004). Pop-in Events Induced by Spherical Indentation in Compound Semiconductors, *Journal of Materials research*, Vol. 19, No. 1, pp. 380-386, ISSN 0884-291

Bradby, J. E.; Williams, J. S., Wong-Leung, J., Swain, M. V. & Munroe, P. R. (2002). Nanoindentation-induced Deformation of Ge, *Applied Physics Letters*, Vol. 80, No. 15, pp. 2651-2653

Chang, L. & Zhang, L. C. (2009). Deformation Mechanisms at Pop-out in Monocrystalline Silicon under Nanoindentation, *Acta Materialia*, Vol. 57, No. 7, pp. 2148-2153, ISSN 1359-6454

Cheng, Y. T. & Cheng, C. M. (1998). Further Analysis of Indentation Loading Curves: Effects of Tip Tounding on Mechanical Property Measurements. *Journal of Materials research*, Vol. 13 No. 4, pp. 1059-1064, ISSN 0884-2914

Chiu, Y. L. & Ngan, A. H. W. (2002). Time-dependent Characteristics of Incipient Plasticity in Nanoindentation of a Ni3Al Single Crystal, *Acta Materialia*, Vol. 50, No. 6, pp. 1599-1611, ISSN 1359-6454

Constantinides, G.; Silva, E. C. C. M., Blackman, G. S. & Vliet, K. J. V. (2007). Dealing with Imperfection: Quantifying Potential Length Scale Artefacts From Nominally Spherical Indenter Probes, *Nanotechnology*, Vol. 18, No. 30, pp. 305503 1-14, ISSN 0957-4484

Cross, G. L; Schirmeisen, W., A., Grutter, P. & Durig, U. T. (2006). Plasticity, Healing and Shakedown in Sharp-asperity Nanoindentation, *Natual Materials*, Vol. 5, No. 5, pp. 370-376, ISSN 1476-1122

Doerner, M. F. & Nix, W. D. (1986). A Method for Interpreting the Data from Depth-sensing Indentation Instruments, *Journal of Materials research*, Vol. 1, No. 04, pp. 601-609, ISSN 0884-2914

Fisher-Cripps, A. C. (2002). *Nanoindentation*, ISBN 1441998713, 9781441998712, New York: Springer-Verlag.

Gane, N. & Bowden, F. P. (1968). Microdeformation of Solids, *Journal of Applied Physics*, Vol. 39, No. 3, pp. 1432-1435, ISSN 0021-8979

Gerberich, W. W.; Nelson, J. C., Lilleodden, E. T., Anderson, P. & Wyrobek, J. T. (1996). Indentation Induced Dislocation Nucleation: The Initial Yield Point, *Acta Materialia,* Vol. 44, No. 9, pp. 3585-3598, ISSN 1359-6454

Gouldstone, A.; Koh, H.-J., Zeng, K.-Y., Giannakopoulos, A. E. & Suresh. S. (2000). Discrete and Continuous Deformation during Nanoindentation of Thin Films, *Acta Materialia,* Vol. 48, No. 9, pp. 2277-2295, ISSN 1359-6454

Haq, A. J.; Munroe, P. R., Hoffman, M., Martin, P. J. & Bendavid. A. (2007). Deformation Behaviour of DLC Coatings on (111) Silicon Substrates, *Thin Solid Films,* Vol. 516, No. 2–4, pp. 267-271, ISSN 0040-6090

Hasche, K.; Herrmann, K., Pohlenz, F. & Thiele, K. (1998). Determination of the Geometry of Microhardness Indenters with a Scanning Force Microscope, *Measurement Science and Technology*, Vol. 9, pp. 1082-1086, ISSN 0057-0233

Herrmann, K.; Hasche, K., Pohlenz, F. & Seeman, R. (2001). Characterisation of the Geometry of Indenters Used for the Micro- and Nanoindentation Method, *Measurement,* Vol. 29, pp. 201-207, ISSN 0263-2241

Jang, J.; Lance, M. J., Wen, S., Tsui, T. Y. & Pharr, G. M. (2005). Indentation-Induced Phase Transformation in Silicon: Influences of Load, Rate and Indenter Angle on the Transformation Behavior, *Acta Materialia,* Vol. 53, pp. 1759-1770, ISSN 1359-6454

Johnson, K. L. (1999). *Contact Mechanics,* ISBN-13, 978-0521347969, Cambridge university Press.

Juliano, T.; Domnich, V. & Gogotsi, Y. (2004). Examining Pressure-induced Phase Transformations in Silicon by Spherical Indentation and Raman Spectroscopy: A Statistical Study, *Journal of Materials research,* Vol. 19, No. 10, pp. 3099-3108, ISSN 0884-2914

Jungk, J. M.; Boyce, B. L., Buchheit, T. E., Friedmann, T. A., Yang, D. & Gerberich, W. W. (2006). Indentation Fracture Toughness and Acoustic Energy Release in Tetrahedral Amorphous Carbon Diamond-like Thin Films, *Acta Materialia,* Vol. 54, No. 15, pp. 4043-4052, ISSN 1359-6454

Kelchner, C. L.; Plimpton, S. J. & Hamilton, J. C. (1998). Dislocation Nucleation and Defect Structure during Surface Indentation, *Physical Review B,* Vol. 58, No. 17, pp. 11085-11088

Kiely, J. D. & Houston, J. E. (1998). Nanomechanical Properties of Au (111), (001), and (110) Surfaces, *Physical Review B,* Vol. 57, No. 19, pp. 12588-12594

Kiener, D.; Durst, K., Rester, M. & Minor, A.M. (2009). Revealing Deformation Mechanisms with Nanoindentation, *JOM*, Vol. 61, No. 3, pp. 14–23, ISSN 1047-4838

Lee, W. S. & Fong. F. J. (2008). Microstructural Study of Annealed Gold–silicon Thin Films under Nanoindentation, *Materials Science and Engineering: A,* Vol. 475, No. 1–2, pp. 319-326, ISSN 0291-5093

Levine, L. E.; Larson, B. C., Yang, W., Kassner, M. E., Tischler, J. Z., Deloas-Reyer, M. A., Fields R. J. & Liu, W. J. (2006). X-ray Microbeam Measurements of Individual Dislocation Cell Elastic Strains in Deformed Single Crystal Copper, *Nature Materials,* Vol. 5, pp. 619-622, ISSN 1476-1122

Levine, L. E.; Geantil, P., Larson, B. C., Tischler, J. Z., Kassner, M. E., Liu, W. J., Stoudt, M. R. & Tavazza, F. (20011). Disordered Long Range Internal Stresses in Deformed Copper

and the Mechanisms Underlying Plastic Deformation. *Acta Materialia,* Vol. 59, pp. 5803-5811, ISSN 1359-6454

Li, J.; Van Vliet, K. J., Zhu, T., Yip, S. & Suresh, S. (2002). Atomistic Mechanisms Governing Elastic Limit and Incipient Plasticity in Crystals, *Nature,* Vol. 418, No. 6895, pp. 307-310, ISSN 0028-0836

Li, T. L; Gao, Y. F., Bei, H., George, E. P. (2011). Indentation Schmid Facor and Orientation Dependence of Nanoindentation Pop-in Behavior of NiAl Single Crystals. *Journal of the Mechanics and Physics of Solids,* Vol. 59, pp. 1147-1162, ISSN 0022-5096.

Lide, D. (2007). *CRC Handbook of Chemistry and Physics,* 87th Edition edition.

Lorenz, D.; Zeckzer, A., Hilpert, U., Grau, P., Johansen, H. & Leipner, H. S. (2003). Pop-in Effect as Homogeneous Nucleation of Dislocations during Nanoindentation. *Physica B: Condensed Matter,* Vol. 67, No. 17, pp. 172101-1-172101-4, ISSN 0163-1829

Ma, L. & Levine, L. E. (2007). Effect of the Spherical Indenter Tip Assumption on Nanoindentation, *Journal of Materials Research,* Vol. 22, No. 6, pp. 1656-1661, ISSN 0884-2914

Ma, L.; Morris, D. J., Jennerjohn, S. L., Bahr, D. F. & Levine. L. E. (2009). Finite Element Analysis and Experimental Investigation of the Hertzian Assumption on the Characterization of Initial Plastic Yield, *Journal of Materials Research,* Vol. 24, No. 3, pp. 1059-1068, ISSN 0884-2914

Ma, L.; Morris, D. J., Jennerjohn, S. L., Bahr, D. F. & Levine, L. E. (2012). The role of probe shape on the initiation of metal plasticity in nanoindentation. *Acta Materialia,* (in press, http://dx.doi.org/10.1016/j.actamat.2012.05.026), ISSN 1359-6454

Mason, J.K.; Lund, A.C. & Schuh, C.A. (2006). Determining the Activation Energy and Volume for the Onset of Plasticity During Nanoindentation, *Physics Review B,* Vol. 73, No. 5, pp. 054102 1-14, ISSN 1098-0121

Mao. W. G.; Shen, Y. G. & Lu, C. (2011). Deformation Behavior and Mechanical Properties of Polycrystalline and Single Crystal Alumina During Nanoindentation, *Scripta Materialia,* Vol. 65 pp. 127-130, ISDN 1359-6462

Nix, W.D., Greer, J.R., Feng, G. & Lilleodden, E.T. (2007). Deformation at the Nanometer and Micrometer Length Scales: Effects of Strain Gradients and Dislocation Starvation, *Thin Solid Films,* Vol. 515, pp. 3152–3157

McElhaney, K. W.; Vlassak, J. J. & Nix, W. D. (1998). Determination of Indenter Tip Geometry and Indentation Contact Area for Depth-sensing Indentation Experiments, *Journal of Materials Research,* Vol. 13, pp. 1300–1306, ISSN 0884-2914

McMinis, J.; Crombez, R., Montalvo, E. & Shen, W. (2007). Determination of the Cross-sectional Area of the Indenter in the Nano-indentation Tests, *Physica B,* Vol. 391, pp. 118-123, ISSN 0921-4526

Minor, A. M.; Lilleodden, E. T., Stach, E. A. & Morris, J. J. W. (2004). Direct Observations of Incipient Plasticity during Nanoindentation of Al, *Journal of Materials research,* Vol. 19, No. 1, pp. 176-182, ISSN 0884-2914

Minor, A. M.; Syed Asif, S. A., Shan, Z., Stach, E. A., Cyrankowski, E., Wyrobek, T. J. & Warren, O. L. (2006). A New View of the Onset of Plasticity During the

Nanoindentation of Aluminium, *Natual Materials,* Vol. 5, No. 9, pp. 697-702, ISSN 1476-1122

Misra, R. D. K.; Zhang, Z., Jia, Z., Somani, M. C. & Karjalainen, L. P. (2010). Probing Deformation Processes in Near-defect Free Volume in High Strength–high Ductility Nanograined/Ultrafine-grained (NG/UFG) Metastable Austenitic Stainless Steels, *Scripta Materialia,* Vol. 63, No. 11, pp. 1057-1060, ISSN 1359-6462

Morris, D. J. (2009). Cleaning of Diamond Nanoindentation Probes with Oxygen Plasma and Carbon Dioxide Snow, *Review of Scientific Instruments,* Vol. 80, No. 12, pp. 126102 1-3, ISSN 0034-6748

Morris, D. J.; Myers, S. B. & Cook, R. F. (2004). Sharp Probes of Varying Acuity: Instrumented Indentation and Fracture Behavior, *Journal of Materials research,* Vol. 10, No. 01, pp. 165-175, ISSN 0884-2914

Munoz-Paniagua, D. J.; McDermott, M. T., Norton, P. R. & Tadayyon, S. M. (2010). Direct Tip Shape Determination of a Berkovich Indenter: Effect on Nanomechanical Property, *IEEE Transactions on Nanotechnology*, Vol. 9, No. 4, pp. 487-493, ISSN 1536-125X

Ogata, S.; Li, J., Hirosaki, N., Shibutani, Y. & Yip, S. (2004). Ideal Shear Strain of Metals and Ceramics, *Physics Review B*, Vol. 70, pp. 104104, ISSN 1098-0121

Oliver, W. C. & Pharr, G. M. (1992). An Improved Technique for Determining Hardness and Elastic Modulus Using Load and Displacement Sensing Indentation Experiments, *Journal of Materials research,* Vol. 7, No. 6, pp. 1564-1583, ISSN 0884-2914

Oliver, W. C. & Pharr, G. M. (2004). Measurement of Hardness and Elastic Modulus by Instrumented Indentation: Advances in Understanding and Refinements to Methodology, *Journal of Materials research,* Vol. 19, No. 1, pp. 3-20, ISSN 0884-2914

Page, T. F.; Oliver, W. C. & McHargue, C. J. (1992). The deformation Behavior of Ceramic Crystals Subjected to Very Low Load (nano)Indentations, *Journal of Materials research,* Vol. 7, No. 2, pp.450-473, ISSN 0884-2914

Pratt, J. R.; Kramar, J. A., Newell, D. B. & Smith, D. T. (2005). Review of SI Traceable Force Metrology for Instrumented Indentation and Atomic Force Microscopy. *Measurement Science and Technology,* Vol. 16, No. 11, pp. 2129-2137, ISSN 0291-5093

Rajulapati, K. V.; Biener, M. M., Biener, J. & Hodge, A. M. (2010). Temperature Dependence of the Plastic Flow Behavior of Tantalum, *Philosophical Magazine Letters*, Vol. 90, No. 1, pp. 35-42, ISSN 0950-0839

Ruffell, S.; Bradby, J. E., Williams, J. S. & Munroe, P. (2007). Formation and Growth of Nanoindentation-induced High Pressure Phases in Crystalline and Amorphous Silicon, *Journal of Applied Physics,* Vol. 102, No. 6, pp. 063521-063528, ISSN 0021-8979

Schuh, C. A. & Lund, A. C. (2004). Application of Nucleation Theory to the Rate Dependence of Incipient Plasticity during Nanoindentation, *Journal of Materials research,* Vol. 19, No. 7, pp. 2152-2158, ISSN 0884-2914

Schuh, C. A.; Mason, J. K. & Lund, A. C. (2005). Quantitative Insight into Dislocation Nucleation from High-temperature Nanoindentation Experiments, *Nature Materials,* Vol. 4, No. 8, pp. 617-621, ISSN 1476-1122

Shim, S.; Bei, H., George, E. P. & Pharr, G. M. (2008). A Different Type of Indentation Size Effect, *Scripta Materialia,* Vol. 59, No. 10, pp. 1095-1098, ISSN 1359-6462

Smith, D. T.; Pratt, J. R. & Howard, L. P. (2009). A Fiber-optic Interferometer with Subpicometer Resolution for dc and Low-frequency Displacement Measurement, *Review of Scientific Instruments,* Vol. 80, pp. 035105, ISSN 0034-6748

Song, J.-F.; Low, S., Pitchure, D., Germak, A., DeSogus, S., Polzin, T., Yang, H.-Q., Ishida, H., & Barbato, G. (1997). Establishing a World-wide Unified Rockwell Hardness Scale with Metrological Traceability, *Metrologia,* Vol. 34, pp. 331-342, ISSN 0026-1394

Suresh, S.; Nieh, T.G. & Choi, B.W. (1999). Nano-indentation of Copper Thin Films on Silicon Substrates, *Scripta Materialia,* Vol. 41, pp. 951–957, ISSN 1359-6462

Szlufarska, I.; Kalia, R. K., Nakano, A. & Vashishta, P. (2007). A Molecular Dynamics Study of Nanoindentation of Amorphous Silicon Carbide, *Journal of Applied Physics,* Vol. 102, No. 2, pp. 023509 1-9, ISSN 0021-8979

Tschopp, M.A. & McDowell, D.L. (2005). Influence of Single Crystal Orientation on Homogeneous Dislocation Nucleation Under Uniaxial Loading, *Journal of the Mechanics and Physics of Solids,* Vol. 56, pp. 1806–1830, ISSN 0022-5096

Tschopp, M.A.; Spearot, D.E. & McDowell, D.L. (2007). Atomistic Simulations of Homogeneous Dislocation Nucleation in Single Crystal Copper. *Modelling and Simulation in Materials Science and Engineering,* Vol. 15, pp. 693–709, ISSN 0965-0393

Tyulyukovskiy, E. & N. Huber. (2007). Neural Networks for Tip Correction of Spherical Indentation Curves from Bulk Metals and Thin Metal Films, *Journal of the Mechanics and Physics of Solids,* Vol. 55, No. 2, pp. 391-418, ISSN 0022-5096

Vadalakonda, S.; Banerjee, R., Puthcode, A. & Mirshams, R. (2006) Comparison of Incipient Plasticity in bcc and fcc Metals Studied Using Nanoindentation, *Materials Science and Engineering A,* Vol. 426, No. 1-2, pp. 208-213, ISSN 0921-5093

Van Vliet, K. J.; Li, J., Zhu, T., Yip, S. & Suresh, S. (2003). Quantifying the Early Stages of Plasticity through Nanoscale Experiments and Simulations, *Physical Review B,* Vol. 67, No. 10, pp. 104105, ISSN 1098-0121

Vander Voort, G. F. (1984). *Metallorgraphy:Principles and Practice.* New York: McGraw-Hill.

VanLandingham, M. R.; Juliano, T. F. & Hagon, M. J. (2005). Measuring Tip Shape for Instrumented Indentation Using Atomic Force Microscropy, *Measurement Science and Technology,* Vol. 16, pp. 2173-2185, ISSN 0291-5093

Vlassak, J. J.; Ciavarella, M., Barber, J. R. & Wang, X. (2003). The Indentation Modulus of Elastically Anisotropic Materials for Indenters of Arbitrary Shape, *Journal of the Mechanics and Physics of Solids,* Vol. 51, No. 9, pp. 1701-1721, ISSN 0022-5096

Wagner, R. J.; Ma, L., Tavazza, F. & Levine, L. E. (2008). Dislocation Nucleation During Nanoindentation of Aluminum, *Journal of Applied Physics,* Vol. 104, No. 11, pp. 114311-1-114311-4, ISSN 0021-8979

Wang, L.; Bei, H., Li, T. L., Gao, T. F., George, E. P. & Nieh, T. G. (2011). Determining the Activation Energies and Slip Systems for Dislocation Nucleation in Body-Centered Cubic Mo and Face-Centered Cubic Ni Single Crystals, *Scripta Materialia,* Vol. 65, No. 3, pp. 179-182, ISSN 1359-6462

Wang, W.; Jiang, C. B. & Lu, K. (2003). Deformation Behavior of Ni3Al Single Crystals During Nanoindentation, *Acta Materialia,* Vol. 51, pp. 6169-6180, ISSN 1359-6454

Warren, O. L.; Downs, S. A. & Wyrobek, T. J. (2004). Challenges and Interesting Observations Associated with Feedback-controlled Nanoindentation. *Zeitschrift Fur Metallkunde,* Vol. 95, No. 5, pp. 287-296

Yoffe, E. H. (1984). Modified Hertz Theory for Spherical Indentation, *Philosophy magazine A* Vol. 50, No. 6, pp. 813-828, ISSN 0141-8610

Zbib, A. A. & Bahr, D. F. (2007). Dislocation Nucleation and Source Activation during Nanoindentation Yield Points, *Metallurgical and Materials Transactions A-Physical Metallurgy and Materials Science,* Vol. 38A, No. 13, pp. 2249-225, ISSN 1073-5623